Article:
Fakhar, Z, Hejazi, L, Tabatabai, SA et al. (2021) Discovery of novel heterocyclic amide-based inhibitors: an integrative in-silico approach to targeting soluble epoxide hydrolase. Journal of Biomolecular Structure and Dynamics, 40 (15). pp. 7114-7128. ISSN: 0739-1102

https://doi.org/10.1080/07391102.2021.1894987

Discovery of Novel Heterocyclic Amide-Based Inhibitors: An Integrative *in-silico* Approach to Targeting Soluble Epoxide Hydrolase

Zeynab Fakhar*[,1], Leila Hejazi[2], Sayyed Abbas Tabatabai[2] and Orde Q. Munro*[,1]

[1]Molecular Sciences Institute, School of Chemistry, University of the Witwatersrand, PO WITS 2050, Johannesburg, South Africa

[2]Department of Pharmaceutical Chemistry, School of Pharmacy, Shahid Beheshti University of Medical Sciences, Tehran, Iran

***Corresponding authors:** zb.fakhar@gmail.com and orde.munro@wits.ac.za

Abstract

Inhibition of soluble epoxide hydrolase (sEH) is considered as an emerging druggable target to reduce blood pressure, improve insulin sensitivity, and decrease inflammation. Despite the availability of different classes of sEH small molecule inhibitors for the potential treatment of hypertension, only a few candidates have reached clinical trials, making the optimal control of blood pressure presently unattainable. This necessity motivated us to explore a series of novel quinazoline-4(3*H*)-one and 4,6-disubstituted pyridin-2(1*H*)-one derivatives targeting sEH enzyme. Herein, comprehensive computational investigations were performed to probe the inhibition efficacy of these potent compounds in terms of inhibitor-enzyme interactions against sEH. In this study, the 39 in-house synthesized compounds were selected. The structure-based pharmacophore modeling was developed based on the crystal structure of sEH with its co-crystallized biologically active inhibitor. The generated hypotheses were applied for virtual screening-based PHASE fitness scores. Docking-based virtual screening workflows were used to generate lead compounds using HTVS, SP and XP based Glide G-score values. The candidate leads were filtered using ADMET pharmacological and physicochemical properties screening. Molecular dynamics simulations were performed to explore the binding affinities of the considered compounds. Our study identified four best candidates from quinazoline-4(3H)-one derivatives, which indicated that a quinazolinone ring serves as a suitable scaffold to develop novel small molecule sEH inhibitors.

Keywords: Soluble Epoxide Hydrolase; quinazoline-4(3*H*)-ones; 4,6-disubstituted pyridin-2(1*H*)-one; Pharmacophore modeling; Virtual screening; Docking workflow; ADMET; MD simulations.

Introduction

Soluble epoxide hydrolase (sEH) is one of the most promising and emerging targets for the development of antihypertensive drugs. Despite the availability of many drugs for the treatment of hypertension, the optimal control of blood pressure is not yet entirely feasible, which may be due to the involvement of various factors on the pathogenesis of hypertension and associated diseases. The sEH enzyme belongs to the α/β-hydrolase family of enzymes exhibiting a high level of selectivity for epoxides of fatty acids. Epoxyeicosatrienoic acids (EETs) that are epoxides of arachidonic acid are responsible for vasodilation in various renal, mesenteric, cerebral, pulmonary & coronary vascular tissues [1]. The EETs are derived from arachidonic acid (AA) and are known as autocrine and paracrine lipid mediators which modulate ion transport and gene expression. Stabilization of EETs has been reported to have various valuable effects on human health such as anti-inflammatory, neuroprotective, analgesic, antihypertensive, and cardioprotective effects [2–7]. However, the rapid hydrolysis of the epoxy functionality of EETs to the corresponding vicinal diols, dihydroxyeicosatrienoic acids (DHETs), by soluble sEH results in a marked reduction of their biological effects [8]. This suggests that the inhibition of sEH stabilizes endogenous EETs and thus preserves their biological activity [9]. Given the potential role of sEH in diminishing EET-induced vasodilation, efforts have been made to inhibit this enzyme [10–14].

The enzyme sEH is expressed in multiple human tissues and is mainly distributed in the liver, brain, kidneys, and endothelium, while also being found at lower levels in other tissues [15,16]. The sEH in mammals is a 125 kDa dimer composed of two identical 62.5 kDa monomers arranged in an anti-parallel fashion. Each sEH monomer has two independent activities including the hydrolase activity in the C-terminal domain (EC 3.3.2.10), and the phosphatase activity, which is localized in the N-terminal domain (EC 3.1.3.76) [17]. Due to the importance of the C-terminal domain in metabolizing EETs as well as in reducing the beneficial effects of EETs, we have focused on the epoxide hydrolysis activity of sEH, **Figure 1**, in this investigation.

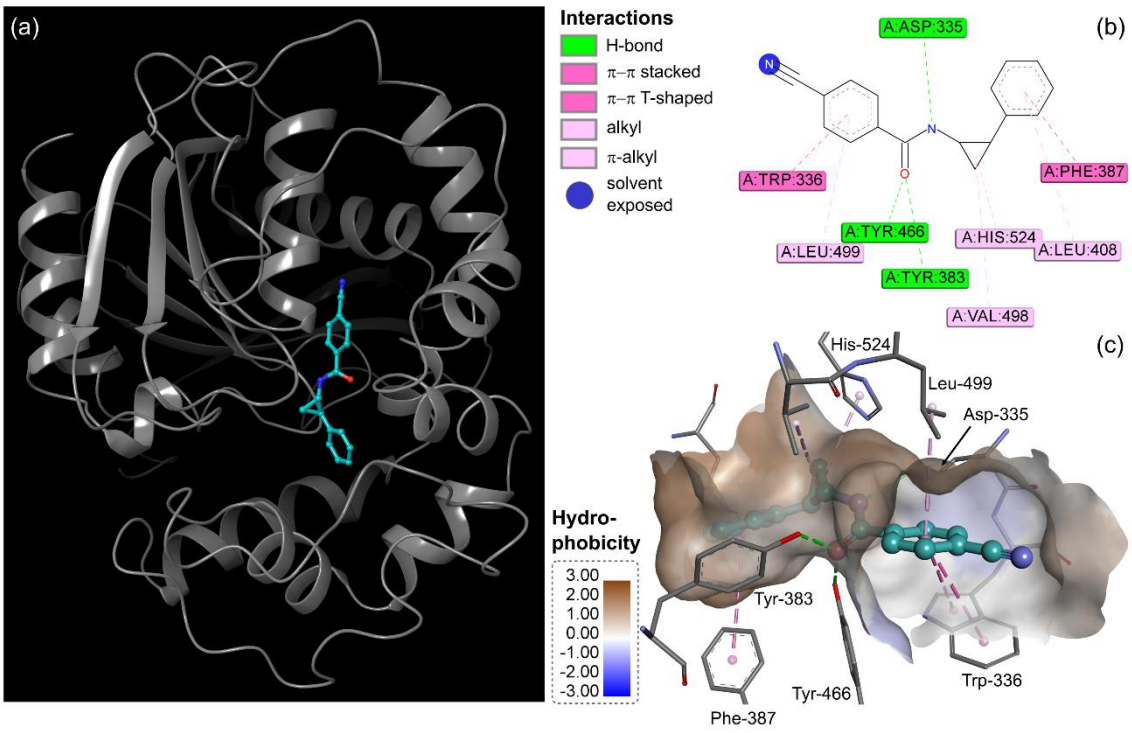

Figure 1. (**a**) Subunit A of the X-ray structure of human sEH (PDB ID: 3ANS) with a noncovalently bound racemic 4-cyano-*N*-(trans-2-phenylcyclopropyl)benzamide inhibitor, **Cpcb**. (**b**) Noncovalent interaction map (2D) displaying significant contacts between the inhibitor and protein within the ligand binding pocket. The hydrogen-bonded catalytic triad (Asp-335, Tyr-383, Tyr-466) is shown in green. (**c**) Location of the benzamide inhibitor (cyan ball and stick model) within the hydrophobic binding pocket of human sEH. The protein surface is colored from high hydrophobicity (brown) to polar (blue) and key pocket residues (labeled) are rendered in cylinder format. The illustration was created from the X-ray structure coordinates of 3ANS [12].

Tanaka *et al.* reported the half maximal inhibitory concentration (IC_{50}) value of 565 nM for racemic 4-cyano-*N*-(trans-2-phenylcyclopropyl)benzamide (**Cpcb**) with human sEH, which confirmed the potency of this type of inhibitor against the enzyme. The X-ray crystal structure of human sEH revealed that the active site of the enzyme is located in an "L"-shaped hydrophobic pocket [18,19], consisting of a catalytic triad Asp-335, Tyr-383 and Tyr-466, as depicted in **Figure 1** [12]. Met-339, His-524 and Gln-384 binding residues located in the hydrophobic pocket are responsible for stabilizing enzyme-inhibitor formation through Van der Waals contacts and hydrogen bonding interactions [12].

To date, many different classes of sEH small molecule inhibitors have been reported but only a few candidate compounds have reached clinical trials. This diverse class of chemotherapeutic agents, which includes ureas, amides, thioamides, thioureas, carbamates, chalcone dioxides as well as acyl hydrazones, exhibit inhibitory activity ranging from the nanomolar- to micromolar

range [10]. However, poor physiochemical properties, rapid metabolism, and low bioavailability are problematic for well-known and potent inhibitors of soluble epoxide hydrolase. Consequently, there is an increasing interest in the development and preclinical evaluation of novel sEH inhibitors. Based on these findings, a number of drug discovery research programs have focused on the development of sEH inhibitors over the last few years [11,20–23].

Recently, novel quinazoline-4(3*H*)-one and 4,6-disubstituted pyridin-2(1*H*)-one derivatives were synthesized and their inhibition of sEH delineated experimentally by Hejazi *et al.* [13,14]. The investigation showed that the newly developed heterocyclic compounds containing a quinazolinone scaffold exhibited improved inhibition efficacy compared with analogues bearing aliphatic substituents, highlighting the fact that the quinazolinone moiety, which is a ubiquitous skeleton in clinically approved drugs, markedly enhances the efficacy of these amide-based sEH inhibitors[14]. Based on this promising work, we were motivated to perform an extensive *in-silico* study to computationally reaffirm the efficacy of these experimentally characterized compounds on sEH enzyme inhibition, especially in terms of their binding affinities.

To address this challenge, an integrated drug discovery approach encompassing 3D structure-based pharmacophore modeling, virtual screening of 39 novel heterocyclic amide-based compounds synthesized by Hejazi *et al.* [13,14], a molecular docking based virtual screening workflow, ADMET pharmacological properties analysis, and molecular dynamics (MD) simulations was undertaken. This efficient and inexpensive strategy aims to provide deeper insights at the molecular level that can be further exploited for the design of potent new lead candidates. The overarching goal is to enhance the probability of a lead candidate within the broader class of compounds reaching pre-clinical trials for the treatment of EET-associated diseases.

Computational Methods

System preparation

The 1.98 Å crystal structure of human soluble epoxide hydrolase (sEH) in complex with a crystalized reference inhibitor (4-cyano-*N*-[(1*S*,2*R*)-2-phenylcyclopropyl]benzamide, **Cpcb**) was retrieved from the Protein Data Bank (PDB ID: 3ANS) [12]. The structure of the enzyme was pre-processed, minimized and refined using the Protein Preparation Wizard [24] implemented in Schrödinger Suite [25]. This step involved eliminating crystallographic waters, adding missing hydrogens/side chain atoms, and assigning the appropriate charge and protonation state of the receptor structure (for pH = 7.0) while considering the appropriate ionization states for the acidic and basic amino acid residues. The prepared macromolecular structure was subjected to energy minimization using the OPLS-2005 force-field [26,27] with a root mean square deviation (RMSD) cut-off value of 0.30 Å to relieve steric clashes among closely-spaced residues arising from the addition of hydrogen atoms.

Preparation of the reference inhibitor and target compounds was accomplished using the LigPrep [28] module of Schrodinger Suite, which adds hydrogen atoms, realistically adjusts bond lengths and angles, and corrects any chirality issues, ionization states, tautomers, stereo chemistries, and ring conformations. Partial charges were assigned to the structures using the OPLS-2005 force-field, and the resulting structures were subjected to energy minimization until their average RMSD reached 0.001 Å. The ionization state was set for pH = 7.0 using the ionization tool within Epik [29].

Preparation of inhibitor-like ligand library

The 39 novel quinazoline-4(3*H*)-one and 4,6-disubstituted pyridin-2(1*H*)-one derivatives recently designed and synthesized by Hejazi *et al*.,[13,14] were considered for further virtual screening analysis. All the compounds were biologically evaluated and showed inhibition activity against sEH enzyme [13,14], **Table S1**.

Identification of 3D-pharmacophore hypotheses

For the structure-based pharmacophore modelling, the PHASE module [30–32] implemented in Maestro 11.6 [33] was used with the default set of seven chemical features: hydrogen bond acceptor (A), hydrogen bond donor (D), hydrophobic contacts (H), negative ionizable group (N), positive ionizable group (P), and aromatic ring (R) to construct the most representative

features of the sEH active sites [34,35]. The six 3D-features were generated using Hypothesis Generation for Energy-Optimized Structure Based Pharmacophores considering the excluded volumes within 5 Å of the refined reference inhibitor for the enzyme [36,37]. Pharmacophore features were selected based on the essential interaction contacts with the key residues of the enzyme accommodating the inhibitor. The resultant pharmacophore features contain the functional groups involved in their bioactivity against the targeted enzyme. The excluded volumes include all atoms within 5 Å of the refined inhibitor for the target.

Virtual Screening of sEH inhibitors

The extracted six pharmacophore features were imported and set as a reference for PHASE-based virtual screening to screen and align the 39 compounds synthesized by Hejazi *et al*. All 39 compounds were aligned based on the highest PHASE fitness score and maximum matched ligand sites, **Table S2**.

Docking-based virtual screening

Molecular docking based virtual screening was performed using Glide [38–40] workflow within Maestro 11.6 [33] to identify the best-fit orientation of the compounds in the active site pocket of sEH (subunit A) to achieve an optimized conformation-based docking score [35].

The appropriate receptor grid was generated based upon a set of center coordinates (X = 26.28, Y = 23.93, Z = 115.85) using two cubical boxes having a common centroid to organize the calculations: a larger enclosing- and a smaller binding box with dimensions of $12 \times 12 \times 12$ Å^3 and $14 \times 14 \times 14$ Å^3, respectively. The grid box was centered on the centroid of the crystallized inhibitor as reference in the complex, which was sufficiently large to explore a larger region of the enzyme structure. The ligands were docked by using the three docking protocols of GLIDE [38–40] which starts with "High throughput Virtual Screening" (HTVS), followed by hit generations using "Standard Precision" (SP), and then lead optimizations in "Extra-Precision" mode (XP), **Table S3** and **S4**. Finally, among the set of 10 poses generated per ligand, the best four compounds and their corresponding poses were selected based on docking scores and XP G-scores.

ADMET properties assessment

The QikProp 5.6 module [41] of Schrodinger was used to predict absorption, distribution, metabolism, excretion and toxicity (ADMET) properties [12,35,42] of the considered compounds to generate the ADMET related descriptors. This protocol predicts significant physicochemical and pharmacokinetic-based descriptors of the compounds based on Lipinski's rule of five [43,44]. ADMET properties of the best lead compounds and the crystalized inhibitor were assessed and analyzed using QikProp 5.6 and considered for the final molecular dynamics (MD) simulations analysis.

Molecular dynamics simulations

Molecular dynamics (MD) simulations considered are as an essential approach to understand the structure-function relationship in biological macromolecules. This method provides detailed information on the fluctuations and conformational changes of a protein as well as energetic information about important protein–ligand interactions [45–49].

AMBER18 [50–52] was used to execute 100 ns MD simulations on all the prepared complexes using the Graphics Processing Unit (GPU) accelerated version of Partial Mesh Ewald Molecular Dynamics (PMEMD) [53,54]. The ff14SB [55] and the general AMBER force fields (GAFF) [56] were employed to parametrize the enzyme and the considered ligands using Leap implemented in AMBER18. The ANTECHAMBER module was used to assign atomic partial charges for the ligands employed in GAFF [56,57]. The system was solvated using the TIP3P [58] explicit water model in a cubic box with a 10 Å distance around the system; Na^+ ions were added randomly to neutralize the complex. The partial Mesh Ewald (PME) method [59] was used to account for the long-range electrostatic forces using a cutoff of 12 Å, and the SHAKE algorithm [60] was used to constrain all the hydrogen atom bonds. Energy minimizations were performed in two stages with 2500 steps of steepest decent minimization followed by 2500 steps of conjugate gradient optimization to remove the bad contacts. The first stage was followed with a harmonic restraint of 500 kcal mol^{-1} A^{-2} on the solute molecule and complete relaxation of ions and water molecules. For the second stage of minimization, the restraints were removed and the whole system was relaxed. Each minimized complex was then gradually heated up from 0 K to 300 K for 200 ps to preserve the solute using a weak harmonic restraint of 10 kcal mol^{-1} A^{-2}. The 50 ps density equilibration with weak restraints followed by the 500 ps constant pressure equilibration at 300 K were both performed at constant pressure using the Berendsen barostat [61]. Ultimately, the production phase of the MD simulation (100 ps) was

performed at a constant temperature of 300 K and constant pressure at 1 atm for all sEH–ligand complexes.

Post-dynamics trajectories analysis

The 100-ns MD trajectories were analyzed to calculate the root mean square deviation (RMSD), root mean square fluctuations (RMSF), and radius of gyration (Rg) using the CPPTRAJ module [62] implemented in AMBER18. Molecular visualizations and plotting were conducted using Maestro 11.6 [33] and Origin Pro 2018 [63].

Binding free energy calculation

The molecular Mechanics/Generalized Born Surface Area (MMGBSA) binding free energy method [64,65] was applied to calculate the relative binding free energies. All water molecules and counter ions were stripped using the CPPTRAJ module. The binding free energy (ΔG_{bind}) was calculated with the MM-GBSA method for each system using the following equations:

$$\Delta G_{bind} = G_{complex} - G_{protein} - G_{ligand} \quad (1)$$

$$\Delta G_{bind} = \Delta E_{gas} + \Delta G_{solvation} - T\Delta S \quad (2)$$

$$\Delta E_{gas} = E_{int} + E_{vdw} + E_{elec} \quad (3)$$

$$E_{int} = E_{bond} + E_{angle} + E_{torsion} \quad (4)$$

$$G_{solvation,GB} = G_{GB} + G_{nonopolar,\ solvation} \quad (5)$$

$$\Delta G_{nonpolar} = \gamma SASA + \beta \quad (6)$$

The gas phase energy (ΔE_{gas}) (eqn 3) is the sum of the internal (E_{int}) (eqn 4), van der Waals (E_{vdW}) and Coulombic (E_{elec}) energies. The solvation free energy is the combination of polar (G_{GB}) and nonpolar ($G_{nonpolar,solvation}$) contributions (eqn 5). It is notable that the G_{GB} polar solvation is calculated using the Generalized Born (GB) solvation model with the dielectric constant 1 for solute and 80.0 for the solvent [66]. The nonpolar free energy contribution was calculated using eqn 6, where the surface tension proportionality constant, γ, and the free energy of nonpolar solvation of a point solute, β, were set to 0.00542 kcal mol^{-1} A^{-2} and 0 kcal mol^{-1}, respectively [67]. The solvent accessible surface area (SASA) was calculated by the linear combination of pairwise overlap method [68].

Per residue free energy decomposition analysis

To evaluate the contributions of individual residues to the total binding free energies, a MM-GBSA per residue free energy decomposition method [67,69,70] was used with the MM-GBSA module of AMBER18. All energy components including van der Waals, electrostatic, polar solvation, and nonpolar solvation contributions were calculated using 1000 snapshots extracted from the last 20 ns of the MD trajectories.

Results and Discussion

In this study, we retrieved 39 compounds from the prior experimental work of Hejazi *et al.* [13,14]; all were selected for virtual screening using 3D-generated pharmacophore hypotheses of the crystallized benzamide inhibitor in complex with the sEH target enzyme (**Figure 1**) [12]. HTVS was used to align the 39 compounds to achieve the best-fit orientation for each derivative within the active site pocket of sEH. Hit generations were effected with GLIDE SP and lead optimization accomplished with GLIDE XP's molecular docking workflow. Four compounds were ultimately selected based on their energetically most favorable docked poses, prior to establishing their ADMET properties with QikProp 5.6, and delineating their dynamic behavior in complex with sEH using 100 ns MD simulations.

Compound library collection

In this study, 39 quinazoline-4(3*H*)-one and 4,6-disubstituted pyridin-2(1*H*)-one derivatives, which are experimentally proven inhibitors of sEH enzyme [12], were considered for *in-silico* investigation. The compound names, two dimensional (2D) structures, and their corresponding experimental affinities for sEH are presented in **Table S1**.

3D Structure-based pharmacophore modeling

Structure-based pharmacophores derived from the three dimensional (3D) structure of a target protein provide detailed and accurate information on ligand binding [71,72]. The best 3D structure-based e-pharmacophores [36,37] were generated using the receptor–ligand pharmacophore generation protocol implemented in PHASE [31], which was performed for the co-crystal benzamide inhibitor inside the active site of sEH specifically to discover potentially important amino acids that are involved in ligand binding (**Figure 2**).

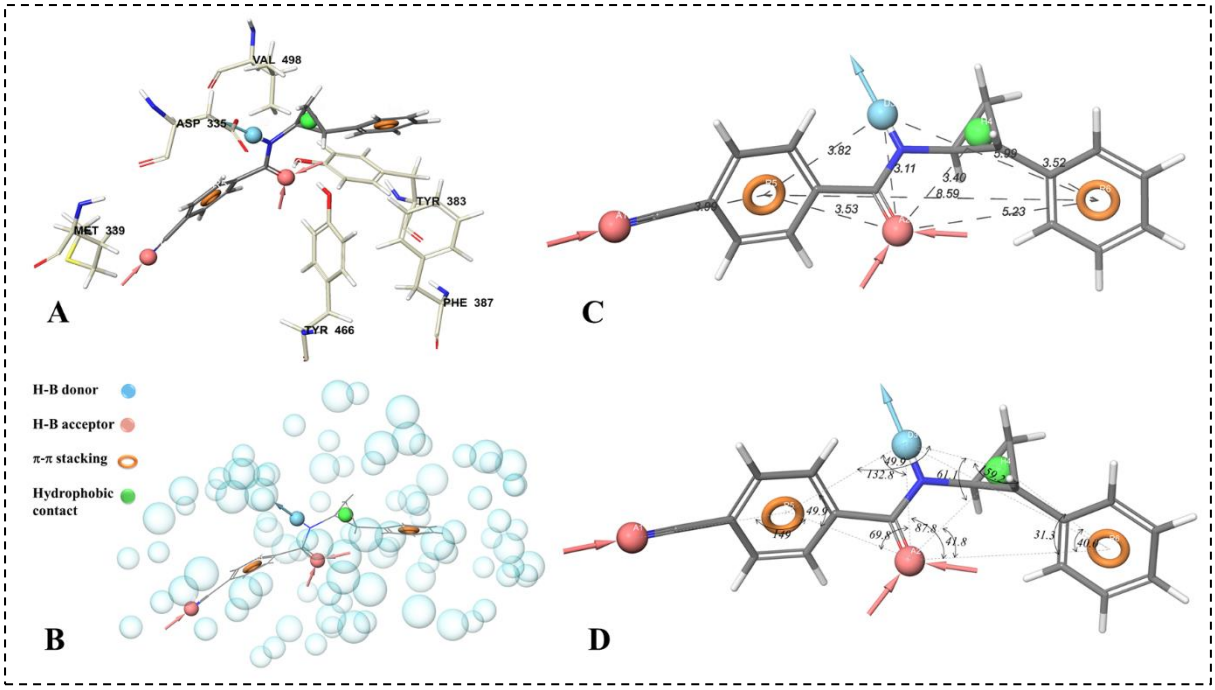

Figure 2. (**a**) 3D pharmacophore features of the co-crystal inhibitor **Cpcb** in complex with sEH. Key: red arrow, hydrogen bond acceptor; blue arrow, hydrogen bond donor; orange ring, aromatic ring; green sphere, hydrophobic contact. (**b**) 3D structure of the inhibitor rendered as a wireframe model and surrounded by excluded volumes represented in light blue bubbles. The six best pharmacophore models are shown at the right side of the figure with key distances (**c**) and angles (**d**) indicated in units of Å and degrees, respectively.

The generated e-pharmacophore for the inhibitor-sEH complex showed six main 3D features, including two H-bond acceptors, one H-bond donor, two π-π stacking motifs (aromatic rings), and one hydrophobic contact. In each pharmacophore model, the red and blue arrows represent the hydrogen bond acceptors and donors, respectively, the orange rings represent aromatic rings, while the green sphere depicts a hydrophobic contact (**Figure 2**). Numerous excluded volumes were also produced in the models to demonstrate the space balancing. The generated H-bond donor motif of the inhibitor establishes the interaction between the N atom of the benzamide moiety and Asp-335. The two H-bond acceptor descriptors include the O atom of the benzamide carbonyl group and the N atom of the cyano functional group. The former accepts hydrogen bonds from Tyr-383 and Tyr-466 (conventional donors) and Met-339 (C–H donor), while the latter is solvent exposed (**Figure 1**). The two π-π stacking features derived from the phenyl and benzamide moieties of the inhibitor culminate in interactions with Phe-387 and Trp-336 of the core binding site residues of sEH. The predicted pharmacophore features contain the key functional groups involved in the bioactivity of the inhibitor (**Cpcb**) toward the target enzyme (sEH).

Virtual screening analysis

The obtained 3D pharmacophore hypotheses of the benzamide inhibitor-sEH complex were used to screen and align the 39 biologically active compounds in the library of interest. Amongst the 388 generated aligned conformations, the highest PHASE fitness score and number of matched sites were then considered to choose the most favorable conformation for docking, based on our virtual screening analysis. The most favorable conformations of the screened compounds are presented in **Table S2**.

Docking-based workflow analysis

A total of 39 aligned compounds (based on the above 3D pharmacophore features) were chosen for docking analysis using GLIDE [38,40] within the Schrödinger Suite package [33]. Three stepwise filtering protocols were used for docking using HTVS, which gave a total of 39 compounds. Subsequent use of GLIDE SP afforded a total of 19 hits (**Table S3** and **S4**). Finally, the best four compounds were filtered using GLIDE XP lead optimization, while only one pose per ligand was retained. The full chemical nomenclature and 2D chemical structures of the four lead compounds, namely **3q**, **3p**, **3d** and **3i**, are presented in **Scheme 1**.

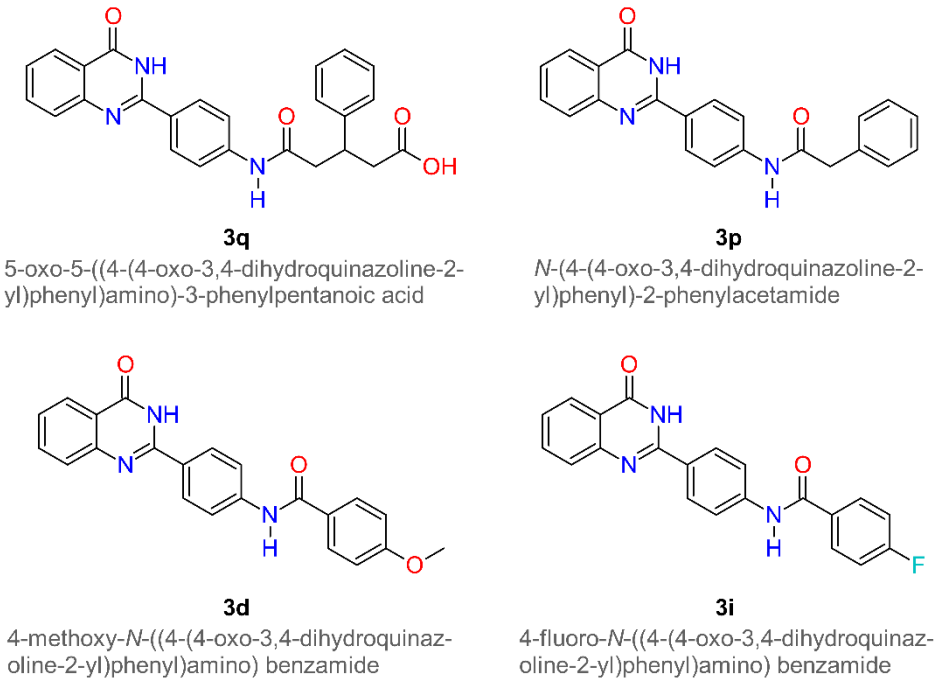

Scheme 1. Full chemical nomenclature and 2D chemical structures of the four GLIDE XP-optimized lead compounds, namely **3q**, **3p**, **3d** and **3i**.

The four lead compounds along with the co-crystal benzamide inhibitor (**Cpcb** in **Figures 1** and **2**), their corresponding Glide G-scores, and their interacting binding site residues are presented in **Table 1**.

Table 1. Summary of the four top lead compounds generated using GLIDE XP docking with their corresponding docking scores and interacting binding site residues.

Entry	Compound	GLIDE G-score (kcal/mol)	Interacting binding site residues
1	**3q**	−12.23	Asp-335, Trp-336, Phe-381, Tyr-383, Gln-384, Leu-408, Tyr-466, Met-469, Leu-499
2	**3p**	−11.40	Asp-335, Trp-336, Met-339, Pro-371, Tyr-383, Tyr-466, Met-469, Val-498, His-524
3	**3d**	−10.15	Phe-267, Asp-335, Trp-336, Tyr-383, Ser-407, Leu-408, Ser-184, Leu-186, Trp-235, Val-267, Leu-268
4	**3i**	–9.84	Phe-267, Asp-335, Trp-336, Leu-499, Tyr-383, Ser-407, Leu-408, Ser-415, Tyr-466, His-524
5	**Cpcb**	–9.92	Asp-335, Trp-336, Tyr-383, Phe-387, Tyr-466, Leu-499

The Glide XP G-scores for the four docked lead compounds **3q**, **3p**, **3d**, **3i**, and the reference inhibitor **Cpcb** (IC_{50}: 565 nM) [12], were −12.23, −11.40, −10.15, –9.84, and –9.92 kcal/mol, respectively. The magnitude of these values is consistent with a strong fit orientation in terms of binding affinities, particularly for compounds **3q**, **3p** and **3d** (**Table 1**). The best poses for the four lead compounds in the binding site cavity of the enzyme are illustrated in **Figure 3** and **S3**. Analogous information for the reference inhibitor **Cpcb** is given in **Figure 1** and **Figure S1**.

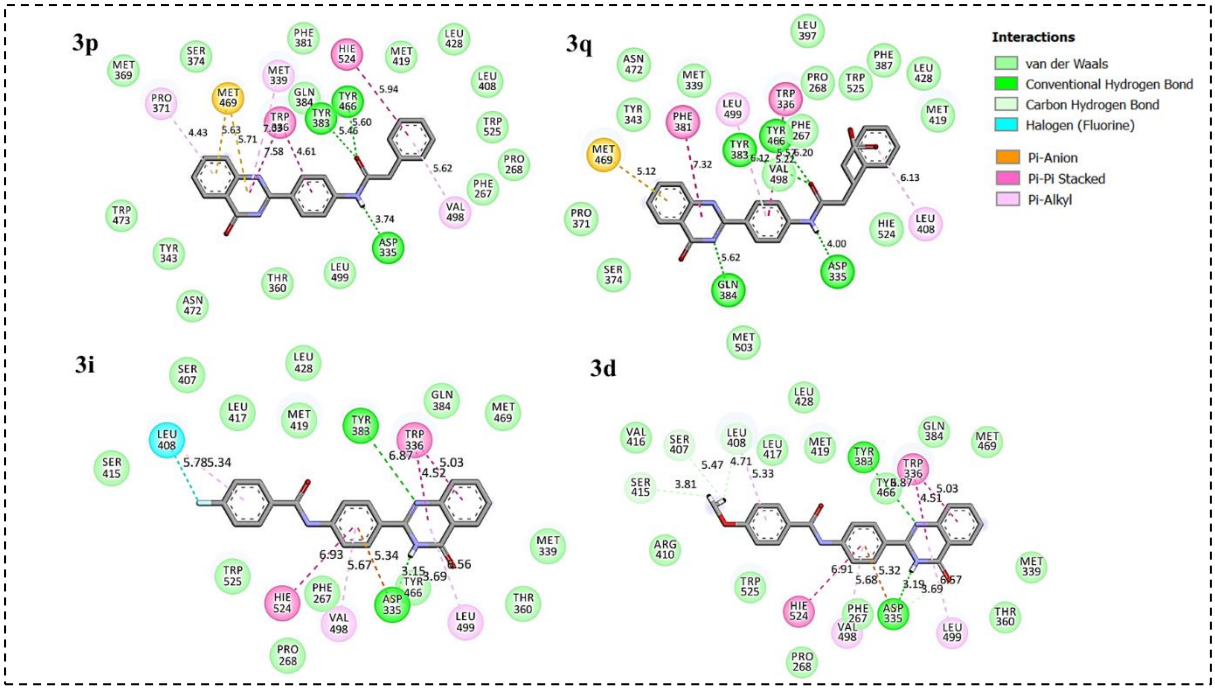

Figure 3. Binding modes for the best poses of the docked complexes **3q**, **3p**, **3d** and **3i** in the active site of sEH. Dark purple lines signify π–π stacking interactions, green lines represent the hydrogen bonding interactions, and orange lines represent the π-anion interactions within the binding pocket.

Several binding site residues within the hydrophobic pocket of sEH confer noteworthy stabilizing interactions with the compounds **3q**, **3p**, **3d**, and **3i** (**Figure 3**), as well as the reference inhibitor **Cpcb** (**Figure 1**). Compound **3q** exhibits hydrogen bonding interactions with Asp-335, Tyr-383, Gln-384, and Tyr-466, two π–π stacking interactions with Trp-336 and Phe-381, and one π-anion interaction involving Met-469. For compound **3p** in complex with sEH, the ligand hydrogen bonds to the two active site tyrosine residues (Tyr-383 and Tyr-466), forms three π–π stacking interactions with Trp-336 and His-524, and two π-anion interactions with Met-469. The binding affinity of compound **3d** for sEH hinges on two hydrogen bonding interactions with Asp-335 and Tyr-383, as well as three π–π stacking interactions with Asp-335, Trp-336, and His-524. For the noncovalent complex **3i**·{sEH}, the ligand is accommodated in the binding pocket by forming two hydrogen bonding interactions with Asp-335 and Tyr-383, four π–π stacking interactions with Trp-336, His-524, and Asp-335, as well as one halogen bonding interaction between the fluorine atom of **3i** and Leu-408. Regarding the X-ray structure of the reference co-crystal benzamide inhibitor **Cpcb** (**Figure 1**), Tyr-383, Tyr-466, Asp-335, Tyr-466, Trp-336, and Phe-387 stabilize the ligand through three hydrogen bonding and three π–π stacking interactions. From **Figure 3**, it is evident that the greater

number of hydrogen bonding interactions with Asp-353, Tyr-383, and Tyr-466 (the key catalytic residues of the enzyme) as well as Gln-384 in unison with the π-anion interaction involving Met-469 were the key factors underpinning a notably stronger binding affinity for the top four lead compounds listed in Table 1. Interestingly, the fluorine atom of **3i** (fluoro-substituted benzamide side chain) diminished the overall docking score for the **3i**·{sEH} complex.

In silico ADME/T properties analysis

Pharmacokinetic properties were predicted using the QikProp module of Schrödinger Suite [41] for the crystallographically-characterized benzamide co-crystal inhibitor [12] and the top four lead compounds (Table 1). These are presented in **Table 2**.

Table2. *In silico* ADMET predictions for the top four docked compounds as well as the known co-crystal inhibitor (**Bzd**) of sEH [12].

Compound	[a]CNS	[b]QPlogS	[c]QPlogBB	[d]QPlogK_{HSA}	[e]HIA	[f]Rule of 5 violations
3q	–2	–6.17	–2.29	0.16	73.74	0
3p	–2	–6.00	–1.10	0.41	100.00	0
3d	–2	–5.74	–1.21	0.30	94.05	0
3i	–2	–5.84	–1.02	0.32	94.66	0
Cpcb [12]	–2	–5.47	–0.67	0.24	100.00	0

[a]Predicted central nervous system activity from –2 (inactive) to +2 (active); [b]Predicted aqueous solubility, S in mol dm^{-3} (acceptable range: −6.5 – 0.5); [c]Predicted brain/blood partition coefficient (acceptable range: –3.0 – 1.2); [d]Prediction of binding to human serum albumin, HSA (acceptable range: –1.5 to +1.5); [e]Predicted percentage human intestinal absorption (<25% is poor and >80% is high). [f]Number of violations of Lipinski's rule of five: compounds that satisfy these rules are considered druglike (maximum 4).

From Table 2, the central nervous system (CNS) activities of all four compounds, as well as the literature co-crystal inhibitor **Cpcb** [12], were predicted as being inactive. The aqueous solubility (QPlogS) and brain/blood partition coefficient (QPlogBB) for all these compounds fell within the accepted ranges for these two properties. The binding to human serum albumin (QPlogK_{HSA}, 0.16–0.41) for all compounds also fell within the approved range. The predicted percentage human intestinal absorption for all compounds amply met the recommended range with all values > 70%, while the number of violations of Lipinski's rule of five for all ligands

was noteworthy at zero. Collectively, the calculated ADMET indices were acceptable and fell within suitable industry-specified ranges for all the compounds investigated.

Molecular dynamics simulations analysis

In this section, 100 ns MD trajectories of the five complexes, namely, **3q**·{sEH}, **3p**·{sEH}, **3d**·{sEH}, **3i**·{sEH}, and **Cpcb**·{sEH} [12] as the control model as well as unbound sEH were analyzed. Different metrics and analyses were applied to investigate the stability and flexibility of the complexes in unison with the contribution made by the studied compounds to target binding in terms of their binding free energies.

Stability and flexibility indices (RMSD/RMSF)

To evaluate the reliability of the MD simulations for the considered complexes as well as unbound sEH, the root mean square deviation (RMSD) of the enzyme's backbone heavy atoms over their 100-ns MD trajectories were analyzed, **Figure 4a**. The RMSD graph shows that the five simulated complexes are considerably well-equilibrated and stabilized, after just 20 ns. The average RMSD values of the backbone atoms for the inhibitor-sEH complexes **3q**·{sEH}, **3p**·{sEH}, **3d**·{sEH}, **3i**·{sEH}, **Cpcb**·{sEH}, and unbound free enzyme were about 1.52, 1.42, 1.62, 1.68, 1.81 and 1.67 Å, respectively. As is evident in **Figure 4a**, all systems showed significant convergence and stabilization in terms of their RMSD metrics after 20 ns, which implies the trajectories were stable and could thus be used reliably for the post-dynamics analyses.

To provide detailed insight into the structural fluctuation and flexibility of different regions of the amino acid residues of sEH enzyme upon uptake of the selected compounds, as well as unbound or native sEH, the per-residue root mean square fluctuation (RMSF) values for the Cα atoms were calculated from the 100-ns MD trajectories, **Figure 4b**. From **Figure 4b**, the inhibitor-enzyme complexes **3q**·{sEH}, **3p**·{sEH}, **3d**·{sEH}, **3i**·{sEH}, **Cpcb**·{sEH}, and unbound native enzyme gave average residue fluctuations of 8.94, 10.28, 9.85, 11.96, 11.61 and 12.45 Å, respectively. According to the RMSF plot, it is evident that the different ligand structures imposed a significant effect on the overall structural flexibility and fluctuations of the protein residues upon binding. For instance, examination of the RMSF plot over the residue range 420-430 shows that there are substantial variations (between 8 and 22 Å) in this region, depending on the structural complexity of the bound inhibitor. Val-422, Leu-428, and Phe-429 are key residues which line the deepest region of the hydrophobic ligand-binding pocket of the

enzyme. Inhibitor **3d** dampens dynamic motion the most (RMSF ~8 Å) for these residues relative to the native enzyme (RMSF ~14 Å), most likely because it penetrates the pocket more deeply by virtue of its somewhat smaller size. Overall, the RMSF amplitudes are predominantly lower in the inhibitor-bound enzyme relative to the native enzyme, as might be anticipated, since uptake of an inhibitor is associated with multiple stabilizing enzyme···inhibitor noncovalent interactions (**Figure 3**). There are, however, exceptions with His-420 showing the highest RMSF value (~22 Å) of any residue in the adduct **3p**·{sEH}. His-420 is surface-exposed and located at the start of the loop that turns inward to ultimately line the hydrophic ligand binding pocket of the enzyme. It is possible that the binding of inhibitor **3p** turns His-420 further outward relative to the other inhbitors, engendering greater dynamic motion for this solvent-exposed residue.

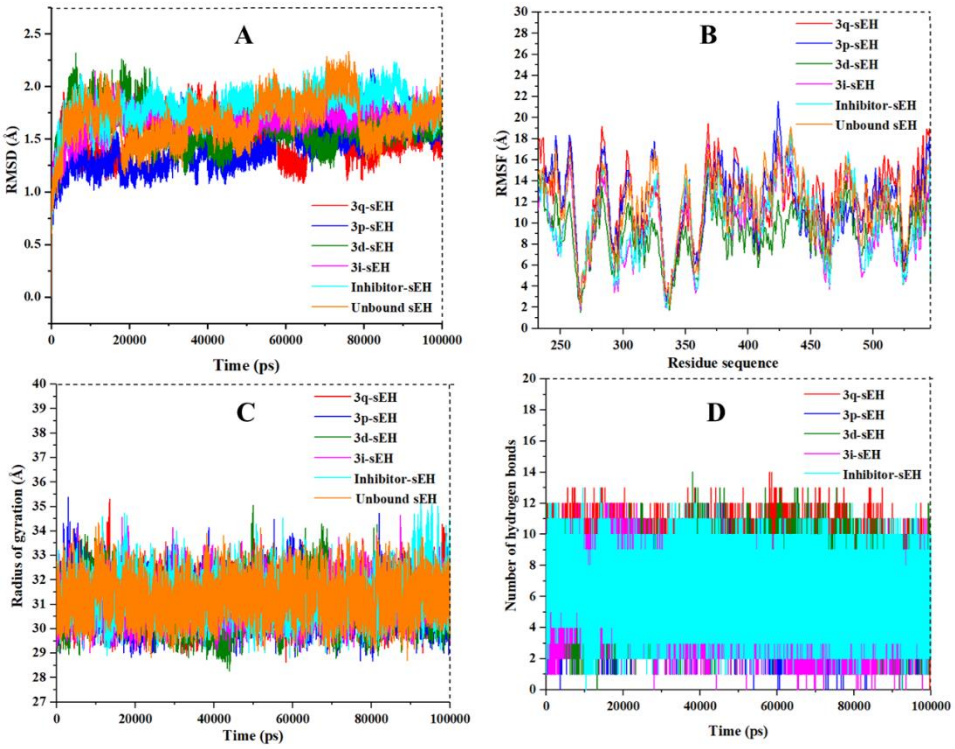

Figure 4. Write a suitable figure caption…

Analysis of the radius of gyration (Rg)

The radius of gyration (Rg) indicates the structural compactness of the protein complex [73]. A mainly random distribution of the radius of gyration values was obtained for native sEH and the complexes **3q**·{sEH}, **3p**·{sEH}, **3d**·{sEH}, **3i**·{sEH}, and **Cpcb**·{sEH} during the 100-ns MD simulations, **Figure 4c**. Notably, the average values of Rg for **3q**·{sEH}, **3p**·{sEH}, **3d**·{sEH}, **3i**·{sEH}, **Cpcb**·{sEH}, and unbound sEH were 31.02, 30.81, 31.14, 30.52, 31.68, 32.22 Å, respectively. The mean Rg values do not vary significantly for the four hit compounds in complex with sEH (**Figure 3**) and all are slightly lower than the mean Rg value obtained for native sEH. This collectively reflects rather moderate conformational changes for the inhibitor-enzyme complexes during the simulations and suggests that the presence of the bound inhibitor dampens the dynamic motion of the macromolecule relative to the ligand-free enzyme. This behavior is certainly expected on the basis of the number of stabilizing noncovalent interactions between the enzyme and each inhibitor (**Figure 3**).

Hydrogen bond analysis

To confirm the overall stability and strength of the interactions of the enzyme-ligand complex [70,74,75], we monitored the intermolecular hydrogen bonds between the enzyme and the bound inhibitor (**Figure 4d**). Intermolecular hydrogen bonding between the protein and the ligand plays a vital role in stabilizing all protein-ligand complexes. The stability of the hydrogen bond network formed between the investigated hit ligands and sEH was evaluated over the course of the 100-ns MD simulation trajectory. Detailed time-dependent information of the hydrogen bonding pattern, specifically the number of intact hydrogen bonds, between the protein and bound ligand is presented in **Figure 4d**.

The average number of intermolecular hydrogen bonds formed between the ligand and the enzyme within the binding pocket of sEH is observed to be 8 and 7 in complexes **3q**·{sEH} and **3p**·{sEH} over the complete 100 ns MD trajectory (**Figure 4d**). However, in the case of **3d**·{sEH}, **3i**·{sEH}, and **Cpcb**·{sEH} the average number of intermolecular hydrogen bonding interactions was 6, 6, and 5, respectively. These observations likely explain the tighter binding interactions and overall more stable complexes (in terms of their binding affinities, Table 1) formed between **3q** and **3p** and sEH.

Binding free energy analysis

To understand the impact of the investigated inhibitors upon complexation by sEH in terms of their binding affinities, the MM-GBSA binding free energy method was utilized to calculate the binding free energies (ΔG_{bind}) and its constituent energy terms for the inhibitor-enzyme complexes (**Table 3**).

Table 3. Binding free energies and constituent energy terms for the top four lead compounds in complex with sEH calculated using the MM-GBSA method. Data for the reference benzamide inhibitor are included and all energy components are in units of kcal/mol.

Complex	ΔE_{vdw}	ΔE_{elec}	ΔG_{gas}	ΔG_{polar}	$\Delta G_{nopolar}$	$\Delta G_{solvation}$	ΔG_{bind}
3q·{sEH}	–54.15	–63.37	–117.52	78.35	–7.07	71.28	–46.23
3p·{sEH}	–51.50	–49.43	–100.94	63.46	–6.73	51.38	–44.21
3d·{sEH}	–49.71	–32.38	–82.09	45.36	–6.04	39.32	–42.78
3i·{sEH}	–46.62	–32.42	–79.04	43.28	–5.66	37.62	–41.42
Cpcb·{sEH}	–35.93	–35.35	–71.28	44.99	–5.35	39.63	–31.65

As presented in **Table 3**, the total binding free energies (ΔG_{bind}) of **3q**·{sEH}, **3p**·{sEH}, **3d**·{sEH}, **3i**·{sEH}, and **Cpcb**·{sEH} were –46.23, –44.21, –42.78, –41.42, and –31.65 kcal/mol, respectively. Consistent with the complex stability order predicted from the number of hydrogen bonds between the inhibitor and enzyme (*vide supra*), **3q**·{sEH}, **3p**·{sEH} gave the lowest exergonic values of ΔG_{bind}.

At this juncture, it is of interest to address the key contributions that each energy component makes to the total binding free energy. It is evident that amongst the studied complexes, the ΔG_{gas} term represents the most favorable energy component contributing to the total ΔG_{bind} value, with the most exergonic values being observed for **3q**·{sEH} (–117.52 kcal/mol) and **3p**·{sEH} (–100.94 kcal/mol). From eqn 3, the Coulombic and van der Waals energy terms will ultimately determine the magnitude of ΔG_{gas} for the same enzyme structure with inhibitors that are structurally similar since the internal energy, which mainly depends on the number of atoms and covalent bonds, will probably span a narrow range. This expectation is indeed borne out by the dominant favorable contributions made by the terms ΔE_{vdw} and ΔE_{elec} to ΔG_{gas} for both **3q**·{sEH} (–54.15 and –63.37 kcal/mol) and **3p**·{sEH} (–51.50 and –49.43 kcal/mol). The important role of dispersion for the binding of the inhibitors is amply demonstrated by the free energy term $\Delta G_{nonpolar}$ (eqn 6) for the complexes **3q**·{sEH} (–7.07 kcal/mol) and **3p**·{sEH}

(–6.73 kcal/mol); these favorable energy components significantly contribute to the highly exergonic calculated ΔG_{bind} values for both **3q** and **3p** with sEH. The energy component data listed in **Table 3** strongly suggest that the ΔE_{vdw}, ΔE_{elec} and $\Delta G_{nonpolar}$ terms collectively dominate the binding affinities of the selected complexes with sEH. The significantly lower value of ΔG_{bind} for the reference complex (**Cpcb**·{sEH}) relative those involving the four lead quinazoline-4(3H)-one derivatives largely reflects the notably poorer ΔE_{vdw} and ΔE_{elec} energy terms for the reference inhibitor.

Residual decomposition energy analysis

The contribution to the total binding free energies of key enzyme residues for **3q**·{sEH}, **3p**·{sEH}, **3d**·{sEH}, **3i**·{sEH}, and **Cpcb**·{sEH} was monitored using a strategy known as per-residue free energy decomposition analysis (FEDA) over the full 100-ns MD simulation trajectory in each case. To achieve this, total binding energies of the inhibitor-enzyme complexes were decomposed into the key residues involved in the substrate/inhibitor binding site of the sEH enzyme (**Figure 5**).

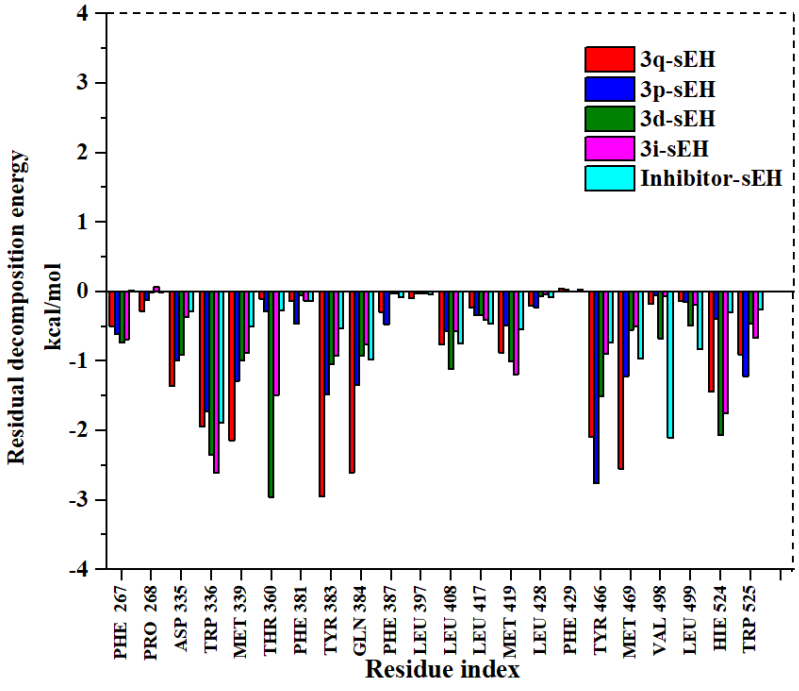

Figure 5. Per-residue decomposition energy of selected compounds with human sEH calculated using the MMGB/SA approach. (Key: **3q**, red; **3p**, blue; **3d**, green; **3i**, magenta; reference benzamide inhibitor, **Cpcb**, cyan).

According to **Figure 5**, the key catalytic triad residues Asp-335, Tyr-383 and Tyr-466 [12] contributed significantly to the total binding energies of both **3q**·{sEH}, **3p**·{sEH}. This observation could be due to the maximum number of hydrogen bonding interactions formed by **3q** and **3p** with these crucial residues (**Figure 3**). Based on experimental work, Hejazi *et al.* [14] predicted that the formation of hydrogen bonds between the inhibitor amide group as the primary pharmacophore and Asp-335, Tyr-383 and Tyr-466 within the hydrophobic pocket of the enzyme's active site, is necessary for a strong inhibitory effect. This structure-based mechanism of action is indeed confirmed in the present *in silico* investigation.

Interestingly, Met-469 showed a more substantial contribution to the binding energies of both **3q**·{sEH} and **3p**·{sEH} relative to **3d**·{sEH}, **3i**·{sEH}, or **Cpcb**·{sEH}. This observation stems from the π-anion interaction between Met-469 and the quinazoline ring of **3q** and **3p** (**Figure 3**). Met-339 located within the hydrophobic substrate-binding pocket of sEH [12] appeared to be another important residue contributing favorably to the total binding energies. The contribution specifically reflects a significant van der Waals contact between Met-339 and the four enzyme-bound lead quinazoline-4(3H)-one derivatives. Again, the stabilizing effect of this interaction was most pronounced for both **3q**·{sEH} and **3p**·{sEH} when compared with **3d**·{sEH}, **3i**·{sEH}, or **Cpcb**·{sEH}. For Gln-384, only **3q**·{sEH} benefitted energetically from an interaction with this residue within the binding pocket, which could be due to the hydrogen bonding interactions between Gln-384 and the NH group of the quinazoline ring of **3q**, as illustrated in **Figure 3**. Finally, His-524 interacted with the enzyme-bound quinazoline-4(3H)-one derivatives through both π-π stacking interactions and van der Waals contacts (**Figure 3**). More specifically, His-524 exhibited π-π stacking interactions with **3p**, **3d**, and **3i** in complex with sEH while noteworthy van der Waals contacts were observed in the enzyme-inhibitor complexes **3q**·{sEH} and **Cpcb**·{sEH}.

Conclusion

In this study, a comprehensive computational inhibitor design approach was followed to identify new lead compounds as inhibitors of soluble epoxide hydrolase (sEH enzyme). 3D-structure based pharmacophore modeling of sEH in complex with a reference racemate benzamide inhibitor (X-ray structure PDB ID: 3ANS) generated six essential pharmacophore features of the inhibitor interacting with the key binding site residues of sEH. The ligand virtual screening based on the six generated pharmacophore descriptors was performed for 39 novel

quinazoline-4(3*H*)-one and 4,6-disubstituted pyridin-2(1*H*)-one derivatives as potent inhibitors of sEH. The 713 screened compounds were obtained using PHASE screen score and their matched ligand sites-based pharmacophore features index. A molecular docking workflow using HTVS, GLIDE SP and GLIDE XP protocols generated the best leads and their corresponding docked poses. The four best lead inhibitors identified in the extra precision (XP) docking protocol were selected based on their docking binding affinities. They were considered further for ADMET prediction-based physicochemical and pharmacokinetic descriptors prior to analysis via 100-ns MD simulations. Our MD simulations revealed that the two highly selective inhibitors of sEH, namely compounds **3q** and **3p**, possessed significant *in silico* binding affinity and would presumably serve as potent inhibitors of the target. Based on our overall observations, compounds **3q** and **3p** could be recommended as potential leads for further development as inhibitors of sEH. In summary, this study provides a useful foundation for designing and developing new potential inhibitors capable of reaching pre-clinical trials to treat EET-associated diseases.

Acknowledgments

ZF would like to acknowledge CHPC server based in Cape Town (South Africa) for computational resources and the National Research Foundation (NRF) through the South African Research Chairs Initiative of the Department of Science and Technology for a postdoctoral research fellowship (running under Grant No 64799 to OQM).

Declaration of Competing Interest

The authors declare that they have no competing interests.

Supplementary information

The following Supplementary material related to this article can be found, in the online version: Table S1, the 2D structure and inhibitory activities of 39 novel quinazoline-4(3*H*)-one and 4,6-disubstituted pyridin-2(1*H*)-one derivatives against sEH; Table S2, the 39 aligned compounds founded on structure-based pharmacophore features using PHASE virtual screening; Table S3, docking-based High Throughput Virtual Screening (HTVS) workflow of the compounds; Table S4, hits generation using GLIDE's docking-based Standard Precision (SP) Screening workflow; Figure S1, binding mode for the best pose of the docked reference inhibitor (4-cyano-*N*-[(1*S*,2*R*)-2-phenylcyclopropyl]benzamide, **Cpcb**) in the active site of sEH.

References

[1] D.J. Behm, A. Ogbonna, C. Wu, C.L. Burns-Kurtis, S.A. Douglas, Epoxyeicosatrienoic acids function as selective, endogenous antagonists of native thromboxane receptors: identification of a novel mechanism of vasodilation., J. Pharmacol. Exp. Ther. 328 (2009) 231–239. https://doi.org/10.1124/jpet.108.145102.

[2] J.H. Capdevila, J.R. Falck, R.C. Harris, Cytochrome P450 and arachidonic acid bioactivation: Molecular and functional properties of the arachidonate monooxygenase, J. Lipid Res. 41 (2000) 163–181.

[3] T.R. Harris, A. Bettaieb, S. Kodani, H. Dong, R. Myers, N. Chiamvimonvat, F.G. Haj, B.D. Hammock, Inhibition of soluble epoxide hydrolase attenuates hepatic fibrosis and endoplasmic reticulum stress induced by carbon tetrachloride in mice, Toxicol. Appl. Pharmacol. 286 (2015) 102–111. https://doi.org/10.1016/j.taap.2015.03.022.

[4] F. Krötz, T. Riexinger, M.A. Buerkle, K. Nithipatikom, T. Gloe, H.Y. Sohn, W.B. Campbell, U. Pohl, Membrane Potential-Dependent Inhibition of Platelet Adhesion to Endothelial Cells by Expoxyeicosatrienoic Acids, Arterioscler. Thromb. Vasc. Biol. 24 (2004) 595–600. https://doi.org/10.1161/01.ATV.0000116219.09040.8c.

[5] N. Tripathi, S. Paliwal, S. Sharma, K. Verma, R. Gururani, A. Tiwari, A. Verma, M. Chauhan, A. Singh, D. Kumar, A. Pant, Discovery of Novel Soluble Epoxide Hydrolase Inhibitors as Potent Vasodilators, Sci. Rep. 8 (2018) 14604–14615. https://doi.org/10.1038/s41598-018-32449-4.

[6] M. Pallàs, S. Vázquez, C. Sanfeliu, C. Galdeano, C. Griñán-Ferré, Soluble epoxide hydrolase inhibition to face neuroinflammation in parkinson's disease: A new therapeutic strategy, Biomolecules. 10 (2020) 703–725. https://doi.org/10.3390/biom10050703.

[7] J. Bellien, R. Joannides, Epoxyeicosatrienoic acid pathway in human health and diseases, J. Cardiovasc. Pharmacol. 61 (2013) 188–196. https://doi.org/10.1097/FJC.0b013e318273b007.

[8] X. Zhao, T. Yamamoto, J.W. Newman, I.H. Kim, T. Watanabe, B.D. Hammock, J. Stewart, J.S. Pollock, D.M. Pollock, J.D. Imig, Soluble Epoxide Hydrolase Inhibition Protects the Kidney from Hypertension-Induced Damage, J. Am. Soc. Nephrol. 15 (2004) 1244–1253.

[9] A.A. Spector, X. Fang, G.D. Snyder, N.L. Weintraub, Epoxyeicosatrienoic acids (EETs): Metabolism and biochemical function, Prog. Lipid Res. 43 (2004) 55–90. https://doi.org/10.1016/S0163-7827(03)00049-3.

[10] H.C. Shen, Soluble epoxide hydrolase inhibitors: A patent review, Expert Opin. Ther. Pat. 20 (2010) 941–956. https://doi.org/10.1517/13543776.2010.484804.

[11] H.C. Shen, B.D. Hammock, Discovery of inhibitors of soluble epoxide hydrolase: A target with multiple potential therapeutic indications, J. Med. Chem. 55 (2012) 1789–1808. https://doi.org/10.1021/jm201468j.

[12] D. Tanaka, Y. Tsuda, T. Shiyama, T. Nishimura, N. Chiyo, Y. Tominaga, N. Sawada, T. Mimoto, N. Kusunose, A practical use of ligand efficiency indices out of the fragment-based approach: Ligand efficiency-guided lead identification of soluble epoxide hydrolase inhibitors, J. Med. Chem. 54 (2011) 851–857. https://doi.org/10.1021/jm101273e.

[13] L. Hejazi, E. Rezaee, S.A. Tabatabai, Design, synthesis and biological activity of 4,6-disubstituted pyridin-2(1h)-ones as novel inhibitors of soluble epoxide hydrolase, Iran. J. Pharm. Res. 18 (2019) 1759–1769. https://doi.org/10.22037/ijpr.2019.112047.13500.

[14] L. Hejazi, E. Rezaee, S.A. Tabatabai, Quinazoline-4(3H)-one derivatives as novel and potent inhibitors of soluble epoxide hydrolase: Design, synthesis and biological evaluation, Bioorg. Chem. 99 (2020) 103736. https://doi.org/10.1016/j.bioorg.2020.103736.

[15] A.E. Enayetallah, R.A. French, M. Barber, D.F. Grant, Cell-specific subcellular localization of soluble epoxide hydrolase in human tissues, J. Histochem. Cytochem. 54 (2006) 329–335. https://doi.org/10.1369/jhc.5A6808.2005.

[16] T.R. Harris, B.D. Hammock, Soluble epoxide hydrolase: Gene structure, expression and deletion, Gene. 526 (2013) 61–74. https://doi.org/10.1016/j.gene.2013.05.008.

[17] A.B. Gurung, B. Mayengbam, A. Bhattacharjee, Discovery of novel drug candidates for inhibition of soluble epoxide hydrolase of arachidonic acid cascade pathway implicated in atherosclerosis, Comput. Biol. Chem. 74 (2018) 1–11. https://doi.org/10.1016/j.compbiolchem.2018.02.019.

[18] M.A. Argiriadi, C. Morisseau, B.D. Hammock, D.W. Christianson, Detoxification of environmental mutagens and carcinogens: Structure, mechanism, and evolution of liver epoxide hydrolase, Proc. Natl. Acad. Sci. U. S. A. 96 (1999) 10637–10642. https://doi.org/10.1073/pnas.96.19.10637.

[19] G.A. Gomez, C. Morisseau, B.D. Hammock, D.W. Christianson, Structure of Human Epoxide Hydrolase Reveals Mechanistic Inferences on Bifunctional Catalysis in Epoxide and Phosphate Ester Hydrolysis, Biochemistry. 43 (2004) 4716–4723. https://doi.org/10.1021/bi036189j.

[20] J. Marino Jr., Soluble Epoxide Hydrolase, a Target with Multiple Opportunities for Cardiovascular Drug Discovery, Curr. Top. Med. Chem. 9 (2009) 452–463. https://doi.org/10.2174/156802609788340805.

[21] G.J. Gross, K. Nithipatikom, Soluble epoxide hydrolase: A new target for cardioprotection, Curr. Opin. Investig. Drugs. 10 (2009) 253–258.

[22] J. Warner, J. Hardesty, K. Zirnheld, C. McClain, D. Warner, I. Kirpich, Soluble Epoxide Hydrolase Inhibition in Liver Diseases: A Review of Current Research and Knowledge Gaps, Biology (Basel). 9 (2020) 124–141. https://doi.org/10.3390/biology9060124.

[23] K.M. Wagner, C.B. McReynolds, W.K. Schmidt, B.D. Hammock, Soluble epoxide hydrolase as a therapeutic target for pain, inflammatory and neurodegenerative diseases, Pharmacol. Ther. 180 (2017) 62–76. https://doi.org/10.1016/j.pharmthera.2017.06.006.

[24] G. Madhavi Sastry, M. Adzhigirey, T. Day, R. Annabhimoju, W. Sherman, Protein and ligand preparation: parameters, protocols, and influence on virtual screening enrichments, J. Comput. Aided. Mol. Des. 27 (2013) 221–234. https://doi.org/10.1007/s10822-013-9644-8.

[25] 2020). Protein Preparation Wizard | Schrödinger, (n.d.). https://www.schrodinger.com/protein-preparation-wizard (accessed April 17, No Title, (n.d.).

[26] E. Harder, W. Damm, J. Maple, C. Wu, M. Reboul, J.Y. Xiang, L. Wang, D. Lupyan, M.K.

Dahlgren, J.L. Knight, J.W. Kaus, D.S. Cerutti, G. Krilov, W.L. Jorgensen, R. Abel, R.A. Friesner, OPLS3: A Force Field Providing Broad Coverage of Drug-like Small Molecules and Proteins, J. Chem. Theory Comput. 12 (2016) 281–296. https://doi.org/10.1021/acs.jctc.5b00864.

[27] W.L. Jorgensen, J. Tirado-Rives, The OPLS [optimized potentials for liquid simulations] potential functions for proteins, energy minimizations for crystals of cyclic peptides and crambin, J. Am. Chem. Soc. 110 (1988) 1657–1666. https://doi.org/10.1021/ja00214a001.

[28] 2020. Schrödinger Release 2020-1: LigPrep, S., LLC, New York, NY, No Title, (n.d.).

[29] 2020. Schrödinger Release 2020-1: Epik, S., LLC, New York, NY, No Title, (n.d.).

[30] S.L. Dixon, A.M. Smondyrev, E.H. Knoll, S.N. Rao, D.E. Shaw, R.A. Friesner, PHASE: a new engine for pharmacophore perception, 3D QSAR model development, and 3D database screening: 1. Methodology and preliminary results., J. Comput. Aided. Mol. Des. 20 (2006) 647–671. https://doi.org/10.1007/s10822-006-9087-6.

[31] S.L. Dixon, A.M. Smondyrev, S.N. Rao, PHASE: a novel approach to pharmacophore modeling and 3D database searching., Chem. Biol. Drug Des. 67 (2006) 370–372. https://doi.org/10.1111/j.1747-0285.2006.00384.x.

[32] 2020. Schrödinger Release 2020-1: Phase, S., LLC, New York, NY, No Title, (n.d.).

[33] 2020. Schrödinger Release 2020-1: Maestro, S., LLC, New York, NY, No Title, (n.d.).

[34] C. Jang, D.K. Yadav, L. Subedi, R. Venkatesan, A. Venkanna, S. Afzal, E. Lee, J. Yoo, E. Ji, S.Y. Kim, M. hyun Kim, Identification of novel acetylcholinesterase inhibitors designed by pharmacophore-based virtual screening, molecular docking and bioassay, Sci. Rep. 8 (2018) 1–21. https://doi.org/10.1038/s41598-018-33354-6.

[35] Z. Fakhar, B. Faramarzi, S. Pacifico, S. Faramarzi, Anthocyanin derivatives as potent inhibitors of SARS-CoV-2 main protease: An in-silico perspective of therapeutic targets against COVID-19 pandemic, J. Biomol. Struct. Dyn. 0 (2020) 1–13. https://doi.org/10.1080/07391102.2020.1801510.

[36] K. Loving, N.K. Salam, W. Sherman, Energetic analysis of fragment docking and application to structure-based pharmacophore hypothesis generation, J. Comput. Aided. Mol. Des. 23 (2009) 541–554. https://doi.org/10.1007/s10822-009-9268-1.

[37] N.K. Salam, R. Nuti, W. Sherman, Novel Method for Generating Structure-Based Pharmacophores Using Energetic Analysis, J. Chem. Inf. Model. 49 (2009) 2356–2368. https://doi.org/10.1021/ci900212v.

[38] R.A. Friesner, J.L. Banks, R.B. Murphy, T.A. Halgren, J.J. Klicic, D.T. Mainz, M.P. Repasky, E.H. Knoll, M. Shelley, J.K. Perry, D.E. Shaw, P. Francis, P.S. Shenkin, Glide: A New Approach for Rapid, Accurate Docking and Scoring. 1. Method and Assessment of Docking Accuracy, J. Med. Chem. 47 (2004) 1739–1749. https://doi.org/10.1021/jm0306430.

[39] R.A. Friesner, R.B. Murphy, M.P. Repasky, L.L. Frye, J.R. Greenwood, T.A. Halgren, P.C. Sanschagrin, D.T. Mainz, Extra Precision Glide: Docking and Scoring Incorporating a Model of Hydrophobic Enclosure for Protein−Ligand Complexes, J. Med. Chem. 49 (2006) 6177–6196. https://doi.org/10.1021/jm051256o.

[40] T.A. Halgren, R.B. Murphy, R.A. Friesner, H.S. Beard, L.L. Frye, W.T. Pollard, J.L. Banks, Glide: a new approach for rapid, accurate docking and scoring. 2. Enrichment factors in database screening., J. Med. Chem. 47 (2004) 1750–1759. https://doi.org/10.1021/jm030644s.

[41] 2020. QikProp, S., LLC, New York, NY, No Title, (n.d.).

[42] H. van de Waterbeemd, E. Gifford, ADMET in silico modelling: towards prediction paradise?, Nat. Rev. Drug Discov. 2 (2003) 192–204. https://doi.org/10.1038/nrd1032.

[43] C.A. Lipinski, F. Lombardo, B.W. Dominy, P.J. Feeney, Experimental and computational approaches to estimate solubility and permeability in drug discovery and development settings., Adv. Drug Deliv. Rev. 46 (2001) 3–26. https://doi.org/10.1016/s0169-409x(00)00129-0.

[44] C.A. Lipinski, Lead- and drug-like compounds: the rule-of-five revolution, Drug Discov. Today Technol. 1 (2004) 337–341. https://doi.org/https://doi.org/10.1016/j.ddtec.2004.11.007.

[45] M. Aminpour, C. Montemagno, J.A. Tuszynski, An Overview of Molecular Modeling for Drug Discovery with Specific Illustrative Examples of Applications, Molecules. 24 (2019) 1693. https://doi.org/10.3390/molecules24091693.

[46] X. Liu, D. Shi, S. Zhou, H. Liu, H. Liu, X. Yao, Molecular dynamics simulations and novel drug discovery., Expert Opin. Drug Discov. 13 (2018) 23–37. https://doi.org/10.1080/17460441.2018.1403419.

[47] C.A. Sotriffer, Molecular Dynamics Simulations in Drug Design BT - Encyclopedic Reference of Genomics and Proteomics in Molecular Medicine, in: Springer Berlin Heidelberg, Berlin, Heidelberg, 2006: pp. 1153–1160. https://doi.org/10.1007/3-540-29623-9_0820.

[48] J.D. Durrant, J.A. McCammon, Molecular dynamics simulations and drug discovery, BMC Biol. 9 (2011) 71. https://doi.org/10.1186/1741-7007-9-71.

[49] M. De Vivo, M. Masetti, G. Bottegoni, A. Cavalli, Role of Molecular Dynamics and Related Methods in Drug Discovery, J. Med. Chem. 59 (2016) 4035–4061. https://doi.org/10.1021/acs.jmedchem.5b01684.

[50] 2018 D.A. Case, I. Y. B.-S., S.R. Brozell, D.S. Cerutti, T.E. Cheatham, III, V.W.D. Cruzeiro, T.A. Darden, R.E. Duke, D. Ghoreishi, M.K. Gilson, H. Gohlke, A.W. Goetz, D. Greene, R Harris, N. Homeyer, S. Izadi, A. Kovalenko, T. Kurtzman, T.S. Lee, S. LeGrand,, AMBER 2018, University of California, San Francisco., (n.d.).

[51] R. Salomon-Ferrer, D.A. Case, R.C. Walker, An overview of the Amber biomolecular simulation package, WIREs Comput. Mol. Sci. 3 (2013) 198–210. https://doi.org/10.1002/wcms.1121.

[52] D.A. Case, T.E. 3rd Cheatham, T. Darden, H. Gohlke, R. Luo, K.M.J. Merz, A. Onufriev, C. Simmerling, B. Wang, R.J. Woods, The Amber biomolecular simulation programs., J. Comput. Chem. 26 (2005) 1668–1688. https://doi.org/10.1002/jcc.20290.

[53] A.W. Götz, M.J. Williamson, D. Xu, D. Poole, S. Le Grand, R.C. Walker, Routine Microsecond Molecular Dynamics Simulations with AMBER on GPUs. 1. Generalized Born, J. Chem. Theory Comput. 8 (2012) 1542–1555. https://doi.org/10.1021/ct200909j.

[54] R. Salomon-Ferrer, A.W. Götz, D. Poole, S. Le Grand, R.C. Walker, Routine Microsecond Molecular Dynamics Simulations with AMBER on GPUs. 2. Explicit Solvent Particle Mesh Ewald, J. Chem. Theory Comput. 9 (2013) 3878–3888. https://doi.org/10.1021/ct400314y.

[55] J.A. Maier, C. Martinez, K. Kasavajhala, L. Wickstrom, K.E. Hauser, C. Simmerling, ff14SB: Improving the Accuracy of Protein Side Chain and Backbone Parameters from ff99SB, J. Chem. Theory Comput. 11 (2015) 3696–3713. https://doi.org/10.1021/acs.jctc.5b00255.

[56] J. Wang, R.M. Wolf, J.W. Caldwell, P.A. Kollman, D.A. Case, Development and testing of a general amber force field., J. Comput. Chem. 25 (2004) 1157–1174. https://doi.org/10.1002/jcc.20035.

[57] J. Wang, W. Wang, P.A. Kollman, D.A. Case, Automatic atom type and bond type perception in molecular mechanical calculations, J. Mol. Graph. Model. 25 (2006) 247–260. https://doi.org/https://doi.org/10.1016/j.jmgm.2005.12.005.

[58] M.F. Harrach, B. Drossel, Structure and dynamics of TIP3P, TIP4P, and TIP5P water near smooth and atomistic walls of different hydroaffinity, J. Chem. Phys. 140 (2014) 174501. https://doi.org/10.1063/1.4872239.

[59] M.J. Harvey, G. De Fabritiis, An Implementation of the Smooth Particle Mesh Ewald Method on GPU Hardware, J. Chem. Theory Comput. 5 (2009) 2371–2377. https://doi.org/10.1021/ct900275y.

[60] J.-P. Ryckaert, G. Ciccotti, H.J.C. Berendsen, Numerical integration of the cartesian equations of motion of a system with constraints: molecular dynamics of n-alkanes, J. Comput. Phys. 23 (1977) 327–341. https://doi.org/https://doi.org/10.1016/0021-9991(77)90098-5.

[61] Y. Lin, D. Pan, J. Li, L. Zhang, X. Shao, Application of Berendsen barostat in dissipative particle dynamics for nonequilibrium dynamic simulation, J. Chem. Phys. 146 (2017) 124108. https://doi.org/10.1063/1.4978807.

[62] D.R. Roe, T.E. Cheatham, PTRAJ and CPPTRAJ: Software for Processing and Analysis of Molecular Dynamics Trajectory Data, J. Chem. Theory Comput. 9 (2013) 3084–3095. https://doi.org/10.1021/ct400341p.

[63] J.G. Moberly, M.T. Bernards, K. V Waynant, Key features and updates for Origin 2018, J. Cheminform. 10 (2018) 5. https://doi.org/10.1186/s13321-018-0259-x.

[64] E. Wang, H. Sun, J. Wang, Z. Wang, H. Liu, J.Z.H. Zhang, T. Hou, End-Point Binding Free Energy Calculation with MM/PBSA and MM/GBSA: Strategies and Applications in Drug Design, Chem. Rev. 119 (2019) 9478–9508. https://doi.org/10.1021/acs.chemrev.9b00055.

[65] J. Srinivasan, T.E. Cheatham, P. Cieplak, P.A. Kollman, D.A. Case, Continuum Solvent Studies of the Stability of DNA, RNA, and Phosphoramidate−DNA Helices, J. Am. Chem. Soc. 120 (1998) 9401–9409. https://doi.org/10.1021/ja981844+.

[66] A. Onufriev, D. Bashford, D.A. Case, Modification of the Generalized Born Model Suitable for Macromolecules, J. Phys. Chem. B. 104 (2000) 3712–3720. https://doi.org/10.1021/jp994072s.

[67] H. Gohlke, C. Kiel, D.A. Case, Insights into protein-protein binding by binding free energy calculation and free energy decomposition for the Ras-Raf and Ras-RalGDS complexes., J.

Mol. Biol. 330 (2003) 891–913. https://doi.org/10.1016/s0022-2836(03)00610-7.

[68] J. Weiser, P.S. Shenkin, W.C. Still, Approximate atomic surfaces from linear combinations of pairwise overlaps (LCPO), J. Comput. Chem. 20 (1999) 217–230. https://doi.org/10.1002/(SICI)1096-987X(19990130)20:2<217::AID-JCC4>3.0.CO;2-A.

[69] Z. Fakhar, T. Govender, G.E.M. Maguire, G. Lamichhane, R.C. Walker, H.G. Kruger, B. Honarparvar, Differential flap dynamics in l,d-transpeptidase2 from mycobacterium tuberculosis revealed by molecular dynamics., Mol. Biosyst. 13 (2017) 1223–1234. https://doi.org/10.1039/c7mb00110j.

[70] P. Gupta, S. Khan, Z. Fakhar, A. Hussain, M.T. Rehman, M.F. AlAjmi, A. Islam, F. Ahmad, M.I. Hassan, Identification of Potential Inhibitors of Calcium/Calmodulin-Dependent Protein Kinase IV from Bioactive Phytoconstituents, Oxid. Med. Cell. Longev. 2020 (2020) 2094635. https://doi.org/10.1155/2020/2094635.

[71] T. Langer, Pharmacophores in Drug Research, Mol. Inform. 29 (2010) 470–475. https://doi.org/10.1002/minf.201000022.

[72] T. Steindl, T. Langer, Influenza virus neuraminidase inhibitors: generation and comparison of structure-based and common feature pharmacophore hypotheses and their application in virtual screening., J. Chem. Inf. Comput. Sci. 44 (2004) 1849–1856. https://doi.org/10.1021/ci049844i.

[73] M.Y. Lobanov, N.S. Bogatyreva, O. V Galzitskaya, Radius of gyration as an indicator of protein structure compactness, Mol. Biol. 42 (2008) 623–628. https://doi.org/10.1134/S0026893308040195.

[74] R.E. Hubbard, M. Kamran Haider, Hydrogen Bonds in Proteins: Role and Strength, ELS. (2010). https://doi.org/doi:10.1002/9780470015902.a0003011.pub2.

[75] T. Mohammad, S. Batra, R. Dahiya, M.H. Baig, I.A. Rather, J.-J. Dong, I. Hassan, Identification of High-Affinity Inhibitors of Cyclin-Dependent Kinase 2 Towards Anticancer Therapy., Molecules. 24 (2019). https://doi.org/10.3390/molecules24244589.